IEEE Access
Multidisciplinary | Rapid Review | Open Access Journal

Received June 5, 2020, accepted June 18, 2020, date of publication June 29, 2020, date of current version July 8, 2020.

Digital Object Identifier 10.1109/ACCESS.2020.3005460

A Dynamic Biometric Authentication Algorithm for Near-Infrared Palm Vascular Patterns

DAVID PALMA[1], (Graduate Student Member, IEEE), FRANCO BLANCHINI[2], (Senior Member, IEEE), GIULIA GIORDANO[3], (Member, IEEE), AND PIER LUCA MONTESSORO[1], (Member, IEEE)

[1]Polytechnic Department of Engineering and Architecture, University of Udine, 33100 Udine, Italy
[2]Department of Mathematics, Computer Science and Physics, University of Udine, 33100 Udine, Italy
[3]Department of Industrial Engineering, University of Trento, 38122 Trento, Italy

Corresponding author: David Palma (palma.david@spes.uniud.it)

This work was supported in part by the European Commission through the European Commission's S3 Operation (European Social Fund (ESF)/2014–2020 Axis 3) within the HEaD–Higher Education and Development Project (Funding Channel 1420AFPLO1) under Grant 1619942002.

ABSTRACT In this paper we apply a novel approach to near-infrared subcutaneous palm vascular pattern authentication. The proposed method relies on a recursive algorithm based on a positive linear dynamical system whose evolution depends on the two matrices representing the vein patterns to be compared. The output of the system reaches a high value when a good matching between the two matrices is observed, otherwise it converges rapidly to zero, even in presence of noise. With respect to another algorithm we recently introduced, this approach achieves not only a better authentication performance but also a drastic reduction in terms of computation time. These improvements are demonstrated by means of extensive experiments conducted on challenging datasets.

INDEX TERMS Biometric authentication, dynamical system, noise-rejection, vascular pattern, vein matching, information security.

I. INTRODUCTION

With the rapid growth in demand for reliable and highly secure human authentication and identification systems, the importance of technological solutions and algorithms in the biometric field is growing along with security awareness [12]. In fact, traditional/conventional authentication methods, consisting in token-based systems that make use of something you have (e.g., ID card), and knowledge-based systems that make use of something you know (e.g., personal identification number or password), are unable to meet the needed reliability and security requirements, while biometric systems make use of physiological (intrinsic) and/or behavioural (extrinsic) traits of individuals, overcoming the security issues affecting the conventional methods for personal authentication [23].

Biometric systems can indeed automatically authenticate or identify subjects in a reliable and fast way and are therefore suitable to be used in a wide range of applications to face the risks of unauthorised logical or physical access and identity theft, as well as new threats such as terrorism or cybercrime [11].

Suitable biometric features for authentication include physiological uniqueness of individuals such as fingerprint, palmprint, hand geometry, face, iris, retina, ear, and behavioural traits such as keystroke dynamics, voice, signature, and gait. Among the listed physiological characteristics, vascular pattern features such as palm veins [4], [29]–[31], finger veins [5], hand veins [14], and hand dorsal veins [19], are an emerging biometric trait that has recently received considerable interest from both the research community and industries [22]. In fact, the subcutaneous vascular pattern of the human body is unique to every individual, even between identical twins [14], does not vary during the course of a person's life, and lies underneath the human skin ensuring confidentiality and robustness to counterfeiting, as opposed to other intrinsic and extrinsic biometric traits that are more vulnerable to spoofing, thus leading to important security and privacy concerns [15].

In addition, since vascular patterns are typically acquired by touch-less devices, they allow for a secure authentication method ensuring high user acceptability without discomfort.

The associate editor coordinating the review of this manuscript and approving it for publication was Vincenzo Conti.

This paper proposes a novel approach to palm vein matching based on a positive linear dynamical system characterised by a high discriminating power and noise-rejection capability. Section II gives an overview of the literature in vein pattern biometrics. Then, Section III illustrates the preprocessing and feature extraction phases aimed at extracting the palm vascular pattern, while Section IV presents our novel algorithm based on the evolution of a dynamical system, and highlights its noise-rejecting properties. The experimental results are reported and discussed in Section V. Finally, conclusions are drawn in Section VI.

II. RELATED WORK

In recent years, the use of palm veins as a trait for automated secure personal authentication has been largely investigated due to their advantages over other biological features.

Veins are part of the network structure of blood vessels underneath the human skin and are almost invisible in normal lighting conditions. However, it is possible to identify the vascular pattern through near-infrared (NIR) illumination with wavelength commonly in the range from 750 nm up to 2000 nm. The incident light in the near-infrared spectrum penetrates into the human biological tissues up to 3-4 mm detecting the vascular pattern underneath the skin [27].

Veins can be distinguished from arteries because arteries carry oxygenated blood that contains oxyhemoglobin, whilst veins carry deoxygenated blood that contains deoxyhemoglobin, which has a different absorbency rate under near-infrared radiations: deoxyhemoglobin absorbs a higher level of NIR radiations, which allows us to detect and isolate vein patterns. As a result of the acquisition in presence of NIR illumination, vascular patterns in raw images appear much darker than all other tissues, which facilitates the feature extraction step for matching.

Various methods for human authentication through palm vascular pattern matching have been proposed in literature. Among them, the work of Zhou and Kumar [31] presents a neighbourhood matching Radon transform (NMRT)-based method aimed at extracting line-like palm vascular features and a Hessian phase-based method to extract palm vein features analysing the eigenvalues of Hessian matrix of the input image. The matching score is computed making use of the Hamming distance. Khan *et al.* [13] use multidirectional representation derived from the nonsubsampled contourlet transform, which is binarised into a hash table. Finally, a L_0-norm approach is used for matching. In another study, Sun and Abdulla [26] introduce an algorithm based on curvelet transform used to obtain curve-like features, whilst Hamming distance is used for matching. The work of Al-juboori *et al.* [1] proposes the use of bank of Gabor filters to extract the vein features, followed by a dimensionality reduction using the Fisher discriminated analysis (FDA) method, and finally the use of the nearest neighbours technique for matching. The study of Kang and Wu [15], instead, utilises an improved local binary pattern method based on mutual foreground for feature extraction and an improved χ^2 distance for matching, whilst the approach proposed in [28] by Wang *et al.*, involves the discriminative local binary pattern (LBP) algorithm for palm vein feature extraction and adopts an improved improved χ^2 distance for verification. Another approach proposed by Kang *et al.* [16], makes use of a local invariant feature extraction technique based on the square root of the scale invariant feature transform (RootSIFT). The work of Ma *et al.* [21] presents an adaptive bidimensional Gabor filter for feature extraction, which are compared using the minimum normalised Hamming distance method, whilst Ahmad *et al.* [2] make use of the wave atom transform (WAT) method for feature extraction and the normalised Hamming distance to compute the matching score. Hong *et al.* [9] make use of a hierarchical classifier based on the fusion of the block dominant orientation code (BDOC) and block-based histogram of oriented gradient (BHOG) features from different spectrum bands (red, green, blue and NIR).

All these techniques can be grouped in three main categories based on the nature of the features used for matching [17]:

- holistic approaches based on multilinear subspace learning: dimensionality reduction techniques are used to project palm vascular images into subspaces aimed at capturing the main features of the palm;
- line/curve matching using vessel extraction based on line-like feature extraction techniques that involve spatial domain filters for line/curve extraction;
- texture based codes, which make use of the orientation of lines as features.

III. HAND PALM IMAGE PROCESSING

Usually, palm print images in the near-infrared band contain not only the blood vessels used to authenticate a person, but also a region of not-interest (e.g., shades, wrist, image background). Moreover, they have different size and orientation and could also be corrupted by noise. All these factors may affect the accuracy in processing and verification performance [33]. Thus, a preprocessing of all palm print images is required to enable the feature extraction phase.

Figure 1 outlines the preprocessing and feature extraction phases illustrating all the main steps involved in the vascular pattern extraction from a raw NIR-based hand palm image. All these steps are detailed in the video included in the additional material (tests #1 and #2).

A. PREPROCESSING

The preprocessing elaboration is required to extract the central region of interest from the input image. As outlined in the Figure 1, the major steps involved in the preprocessing of raw images are: 1) noise reduction, 2) local adaptive binarization, 3) hand shape detection, and 4) ROI coordinate construction and extraction [24].

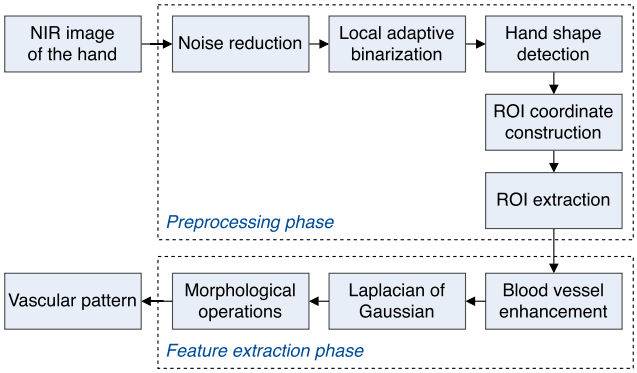

FIGURE 1. Block diagram of the adopted NIR-based hand palm image processing for vascular pattern extraction.

1) NOISE REDUCTION

A noise typically corrupting digital images is the impulse noise [8], [18]. This kind of noise is independent, randomly distributed, and uncorrelated with the image, since it can affect all pixels in the image with the same probability. Hence, a common non-linear spatial filter, i.e. median filter, can be used to remove unwanted information from noisy palmprint images preserving details. In our experiments, the kernel size has been set to 5×5 pixels.

2) LOCAL ADAPTIVE BINARIZATION

It is used to automatically perform a local adaptive clustering-based image thresholding in order to reduce the input gray-level image $I(i, j)$ to a binary image $B(i, j)$. Furthermore, to remove the wrist part of the hand, which can contribute in poor segmentation, the last L pixels on the wrist side of the image are zero-padded as in [15].

3) HAND SHAPE DETECTION

It is achieved by filtering the binary image $B(i, j)$ using Canny's operator [3], which ensures good noise immunity and detects true edges with minimum error [7].

4) ROI COORDINATE CONSTRUCTION AND ROI EXTRACTION

To reduce the influence of rotation, translation, and scaling of the palm, a standard reference system is used to align all the palm images in a standard pose, hence, it is possible to locate the peak and valley points of the palm tracking the distance between the centre of mass of the segmented hand image and the contours of the hand shape. Thus, taking the reference points between the fingers we can construct a reference line to align different hand images and use the middle point between them to detect and extract the 172×172 area of the palmprint's centre without any effort [32].

B. FEATURE EXTRACTION

Since the features are used for matching, feature extraction plays a key role in biometric identification and authentication systems. The proposed feature extraction stage makes use of the following steps: 1) highlighting blood vessels by enhancing contrast and sharpness, 2) Laplacian of Gaussian, and 3) morphological operations. Figure 2 depicts the results of the proposed feature extraction algorithm.

1) BLOOD VESSEL ENHANCEMENT

It highlights blood vessels so that they are easily distinguishable from the background. To correct uneven illumination and to enhance the contrast we combined the Top-Hat and Bottom-Hat transforms, used to detect bright (dark) objects from a varying dark (bright) background. The Top-Hat transform is defined as the difference between the input image I and its morphological opening by a cross shaped structuring element $\mathscr{B} \subseteq \mathbb{Z}^2$:

$$\mathscr{B} = \begin{bmatrix} 0 & 1 & 0 \\ 1 & 1 & 1 \\ 0 & 1 & 0 \end{bmatrix} \tag{1}$$

$$TH = I - (I \circ \mathscr{B}) = I - ((I \ominus \mathscr{B}) \oplus \mathscr{B}) \tag{2}$$

whilst the Bottom-Hat transform is defined as the difference between the closing of the input image $I(i, j)$ by the structuring element $\mathscr{B}$ and the input image itself:

$$BH = (I \bullet \mathscr{B}) - I = ((I \oplus \mathscr{B}) \ominus \mathscr{B}) - I \tag{3}$$

where the opening is obtained by the erosion of $I(i, j)$ by $\mathscr{B}$ followed by dilation of the resulting image by $\mathscr{B}$, and the closing is obtained by the dilation of $I(i, j)$ by $\mathscr{B}$ followed by erosion of the resulting image by $\mathscr{B}$. Then, to remove the bright objects and enhance the black ones that represent the blood vessels, we adopt the Top-Hat and Bottom-Hat transforms as follows:

$$I_o(i, j) = I(i, j) - TH(i, j) - BH(i, j). \tag{4}$$

After this operation, a normalisation [10] is applied to preset the values of mean and variance for all palm images:

$$I_n(i, j) = \begin{cases} \mu_n + \rho & \text{if} \quad I_o(i, j) > \sigma^2 \\ \mu_n - \rho & \text{if} \quad I_o(i, j) \leq \sigma^2 \end{cases} \tag{5}$$

where

$$\rho = \sqrt{\frac{\sigma_n^2 \, (I_o(i, j) - \mu)^2}{\sigma^2}} \tag{6}$$

with $\mu_n = 128$ and $\sigma_n = 40$, determined experimentally.

2) LAPLACIAN OF GAUSSIAN

The Laplacian is a bidimensional isotropic operator used to estimate the second spatial derivative of an image and is commonly used to extract line-like features, since can preserve the pattern suppressing the noise at the same time [26]. In fact, to decrease its sensitivity to noise the operator is applied to an image already smoothed by a bidimensional Gaussian operator $G(i, j)$, whose expression is given by

$$G(i, j) = \exp\left(-\frac{i^2 + j^2}{2\sigma^2}\right). \tag{7}$$

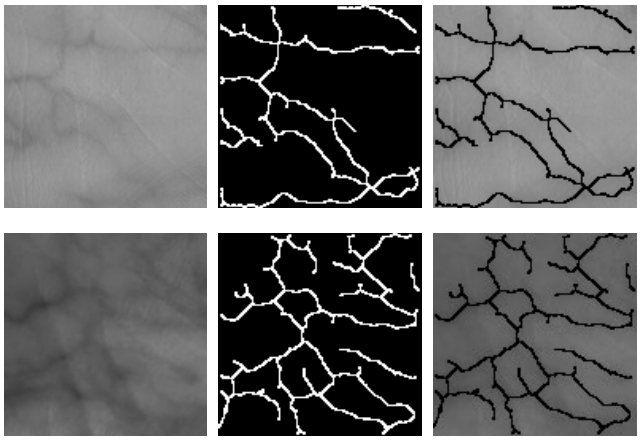

FIGURE 2. Results of the proposed vascular pattern extraction method on PolyU (upper row) and CASIA (lower row) databases: (a) original ROI images, (b) boolean vascular pattern matrices, and (c) original ROI images overlapped with the extracted vascular patterns.

Since convolution and differentiation are the only linear operators involved, it is possible to interchange them:

$$\nabla^2 \left[G(i,j) * I_n(i,j)\right] = \left[\nabla^2 G(i,j)\right] * I_n(i,j). \tag{8}$$

Hence, the Laplacian of Gaussian can be precomputed as:

$$\nabla^2 G(i,j) = \left(\frac{i^2+j^2-2\sigma^2}{\sigma^4}\right) G(i,j). \tag{9}$$

3) MORPHOLOGICAL OPERATIONS

They are aimed at cleaning the vascular pattern image from small objects and noise such as random bright spots on black background and black holes on bright components. To accomplish this goal we use a morphological filter composed of an opening followed by a dilation through a structuring element $\mathscr{B}$ as follows:

$$F = (I \circ \mathscr{B}) \bullet \mathscr{B}. \tag{10}$$

Finally, an iterative thinning transformation is applied to reduce a foreground object to a minimal connected stroke preserving the topology [20], since the final vascular pattern image is homotopically equivalent to the input image. Figure 2 exemplifies the vascular pattern extraction method.

IV. A DYNAMIC ALGORITHM FOR VEIN MATCHING

We discuss here the dynamic algorithm we propose for vein matching, which is a recursive algorithm based on iterative operations on the matrices associated with the images. To have an immediate glimpse on how the algorithm works the reader is invited to take a look at the video included in the additional material. The reader is invited to take a look at the video included in the additional material (tests #3 and #4) to see the time evolution of the dynamic algorithm in both genuine and impostor experiments.

Given two initial images $\bar{X}$ and $\bar{Y}$ of the same size, the recursive algorithm yields a pair of real matrices, X and Y, with the same size as $\bar{X}$ and $\bar{Y}$. The algorithm is initialised as $x_{ij}(0) = \bar{x}_{ij}$ and $y_{ij}(0) = \bar{y}_{ij}$ where $\bar{x}_{ij}$ and $\bar{y}_{ij}$ are the binary values of pixel i, j in the original images $\bar{X}$ and $\bar{Y}$, converted to real (floating point) values. For brevity we refer to the real entries of matrices $X(k)$ and $Y(k)$ as "pixels".

The idea behind the algorithm is to recursively increase the value of a pixel i, j if in the complementary neighbourhood (namely, the neighbourhood of the corresponding pixel i, j in the comparison image) there are pixels with large values. Conversely, if the pixels in the complementary neighbourhood have low values, the value of pixel i, j converges to zero. The algorithm also includes a term that *initially* increases the value of a pixel if the pixels in a proper neighbourhood *in the same image* have large values, and then vanishes with time; it has the effect of initially thickening the relevant patterns.

The two images are processed according to the iterations

$$x_{ij}(k+1) = \lambda x_{ij}(k) + \underbrace{\mu \sum_{hl \in \mathcal{N}_{ij}} y_{hl}(k)}_{\text{cross-matching}} + \underbrace{\nu^k \sum_{hl \in \mathcal{N}_{ij}} x_{hl}(k)}_{\text{initial expansion}} \tag{11}$$

$$y_{ij}(k+1) = \lambda y_{ij}(k) + \underbrace{\mu \sum_{hl \in \mathcal{N}_{ij}} x_{hl}(k)}_{\text{cross-matching}} + \underbrace{\nu^k \sum_{hl \in \mathcal{N}_{ij}} y_{hl}(k)}_{\text{initial expansion}} \tag{12}$$

where $k = 0, 1, \ldots, K-1$, and $\mathcal{N}_{ij}$ is a square neighborhood of the pixel i, j of dimension δ (integer):

$$\mathcal{N}_{ij} = \{h, l : |h-i| \le \delta, \ \ |l-j| \le \delta, \ \ h, l \in \mathbb{Z}\}.$$

At the final step K, to achieve a boolean image, pixels with value smaller than 1 are set to zero whilst pixels with value greater than 1 are saturated to 1, so as to generate the final boolean matrices (images) X' and Y', with

$$x'_{ij} := \{x_{ij}(K) \ge 1\} \ \text{ and } \ y'_{ij} := \{y_{ij}(K) \ge 1\}. \tag{13}$$

Given the size δ of the neighbourhood $\mathcal{N}_{ij}$ and denoting by $\mathrm{n}(\mathcal{N}) = (2\delta+1)^2$ the corresponding number of pixels, the positive parameters λ, μ, ν are selected based on an optimisation procedure.

To limit the search region for the optimisation procedure within a bounded set (see Figure 3), we impose the constraints:

$$0 < \lambda, \mu, \nu < 1 \tag{14}$$

$$\lambda + \nu < 1 \tag{15}$$

$$\frac{1}{2}\mu \cdot \mathrm{n}(\mathcal{N}) < 1 - \lambda < \mu \cdot \mathrm{n}(\mathcal{N}) \tag{16}$$

Since we consider positive parameters, the requirement that $\lambda, \mu, \nu < 1$ in (14) is implied by (15) and (16).

The reasoning behind the introduced constraints can be explained as follows.

- Given (11) and (12) in the absence of cross matching ($\mu = 0$) and of initial expansion terms ($\nu = 0$), $x_{ij}(k)$

and $y_{ij}(k)$ should asymptotically converge to zero: since the iterations become $x_{ij}(k+1) = \lambda x_{ij}(k)$ and $y_{ij}(k+1) = \lambda y_{ij}(k)$, this happens provided that $\lambda < 1$, as in (14).

- The expansion term initially augments x_{ij} (resp. y_{ij}) if the average value of the pixels in the neighbourhood of x_{ij} (resp. y_{ij}) is large. It depends on the factor ν^k, and we set $0 < \nu < 1$ as in (14) so that this initial effect quickly vanishes with time. This is needed because, in the long run, the persistence of this term would make all lines thicker and thicker, leading to false positives.
- The inequality in (15) needs to hold to ensure that, if there is an isolated pixel x_{ij} whose value is initially large, but there are no active pixels in both the neighbourhoods of the image itself and the complementary image, then the pixel value decreases from the very beginning of the iterations, since it evolves as

$$x_{ij}(k+1) = \left(\lambda + \nu^k\right) x_{ij}(k). \tag{17}$$

  With $\nu + \lambda < 1$, such a pixel is therefore quickly cancelled.
- The first inequality in (16) is explained as follows. The cross-matching term increases x_{ij} (resp. y_{ij}) if the average value of the pixels in the complementary neighbourhood is large.
  If $\nu^k \approx 0$, which is ensured for large k in view of (14), we have

$$x_{ij}(k+1) = \lambda x_{ij}(k) + \mu \mathrm{n}(\mathcal{N}) \underbrace{\frac{\sum_{hl \in \mathcal{N}_{ij}} y_{hl}(k)}{\mathrm{n}(\mathcal{N})}}_{\text{average value}} \tag{18}$$

  Hence, $\frac{1}{2}\mu \cdot \mathrm{n}(\mathcal{N}) + \lambda < 1$ implies that, if the average value in the complementary neighbourhood is around or below the half of $x_{ij}(k)$, then x_{ij} gets smaller: $x_{ij}(k+1) < x_{ij}(k)$. Hence, we take the empirical threshold of $x_{ij}(k)/2$ to discriminate whether the complementary neighbourhood has to be considered "populated" or "unpopulated". Conversely, the second inequality in (16), $\mu \cdot \mathrm{n}(\mathcal{N}) + \lambda > 1$, means that if the average value is about or greater than x_{ij}, the complementary region should be consider as "populated" so x_{ij} should get larger: $x_{ij}(k+1) > x_{ij}(k)$. The same holds for $y_{ij}(k)$.

At the end of the iterations, given $x_{ij}(K)$ and $y_{ij}(K)$, the images X' and Y' are produced, where some pixels are set to 0 and others to 1 according to the boolean decision boundary in (13).

The final test is performed on the number of pixels with value 1 (active), which is compared to the initial number. Denoting by $\Sigma(\bar{X})$ and $\Sigma(\bar{Y})$ the number of active pixels in the initial images and by $\Sigma(X')$ and $\Sigma(Y')$ the number of active pixels in the final images, we consider the *matching index* [25]:

$$\alpha = \frac{1}{2}\left[\frac{\Sigma(X')}{\Sigma(\bar{X})} + \frac{\Sigma(Y')}{\Sigma(\bar{Y})}\right]. \tag{19}$$

Similar images will have a large number of surviving pixels (cf. Figure 8 (a) and (c)), hence a large matching index α, while different images will be left with a very small number of nonzero pixels (cf. Figure 8 (b) and (d)), with α considerably small.

Since $\nu^k \to 0$ when $k \to \infty$, asymptotically the recursion becomes identical to that in our algorithm for palmprint matching [25] (which makes use of palmprint features acquired in the visible spectrum rather than in the NIR).

The resulting algorithm works as follows.

Algorithm Vein Matching Index Computation

Input: Boolean images A and B.

Parameters: Number of steps K, positive constants $\lambda, \mu, \nu < 1$, integer neighbourhood amplitude $\delta > 0$.

Outputs: Matching index α.

1) Convert the two input images from boolean into real matrices $X := A$ and $Y := B$.
2) Set $k = 0$.
3) At each iteration, compute the updated values for each pixel in both images according to (11)–(12)
4) Set $k = k + 1$ and, IF $k < K$, GOTO step 3.
5) Generate the boolean matrices $[X', Y']$ as follows: IF $x_{ij} \geq 1$, THEN $x'_{ij} := 1$; ELSE $x'_{ij} := 0$; IF $y_{ij} \geq 1$, THEN $y'_{ij} := 1$; ELSE $y'_{ij} := 0$.
6) Compute the matching index α as in (19).

Therefore, we can formally guarantee that asymptotically the performance is at least as good as with the previous algorithm. Moreover, the new dynamic algorithm has noteworthy advantages.

- The term ν^k provides an initial burst that considerably increases the speed of convergence. Its effect is that of initially enlarging the lines, which is beneficial and very rapidly leads to a situation where the discrimination is possible (see Figure 5).
- The benefits of the joint cross-matching and the initial expansion term are seen in the first iterations, which allows to stop the algorithm at an early stage. Indeed, the best results in terms of discrimination are achieved after few iterations, so waiting any longer is useless (although it does not compromise performance in terms of the matching index, see Figure 5). Stopping the algorithm after few iterations drops the computational time of an order of magnitude (cf. Figure 5) and still allows for very effective authentication.

Given the constraints (15)–(16), the optimal parameter values are chosen based on an experimental campaign in order to maximise the performance.

V. EXPERIMENTAL RESULTS

A. DATABASES USED IN SIMULATION

The performance of the proposed palm vascular pattern authentication system has been tested upon the *PolyU*

multispectral palmprint database [34] and the *CASIA multispectral palmprint database* [35], which are worldwide shared for research purposes and whose details are given in Table 1.

The first database consists of 6 000 palmprint images for each electromagnetic spectrum, captured from 250 subjects by a CCD-based device. All images are 8 bit gray-level of size 352 × 288 pixels at 96 dpi resolution. The second database consists of 1 200 palmprint images for each electromagnetic spectrum, captured from 100 subjects by a CCD-based device. All images are 8 bit gray-level of size 768 × 576 pixels at 96 dpi resolution.

In both databases, for each subject there are palmprint images from both left and right hands captured from people of different ages at different times.

TABLE 1. Specifications of the PolyU and CASIA databases.

	PolyU	CASIA
Subjects	250	100
Samples	24	12
Total	6000	1200
Hand holder	yes	no
Spectrum bands	4	6
Wavelengths [nm]	470, 525, 660, 880	460, 630, 700, 850, 940, WHT

B. PARAMETER OPTIMISATION

Since the proposed approach for matching is based on a linear parameter-dependent system, it is very important to set its internal parameters in order to maximise the system performance. Hence, in this phase we have carried out a one-time parameter tuning procedure which consists of a massive experiment to estimate the values of the parameters λ, μ, and ν that maximise the accuracy of the system.

Thus, given the set $\mathcal{N}$ of nearby points of a generic point $p(x, y)$, it is convenient to set the parameters in accordance with the criteria (14)–(16). To define the set $\mathcal{N}$, it is reasonable to consider a small radius as $\delta = 2$ (which means that the cardinality of $\mathcal{N}$ is equal to $\mathrm{n}(\mathcal{N}) = 25$), since the thickness of blood vessels typically amounts at most to a couple of pixels. This choice allows a perfect coverage of a blood vessel and avoids excessive unwanted overlaps with other blood vessels in the comparison image.

The suitable parameter values, in terms of accuracy and convergence speed, have been found by means of a massive experiment, conducted over a subset of the *CASIA multispectral palmprint database*.

Since it is not possible to thoroughly invesitgate in the convergence domain to find the optimal parameter values, the candidate parameters have been chosen using a Monte Carlo sampling-based approach, generating a large number of pseudo-random points in the space, selecting the only points within the convergence domain, and using the candidate parameters to test the behaviour of the system. Figure 3

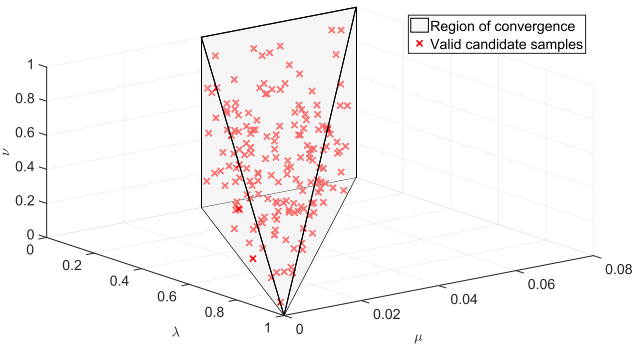

FIGURE 3. Region of convergence of the system bounded by the constraints reported in (14)–(16) (with $\mathrm{n}(\mathcal{N}) = 25$ and $p = 1/2$), and valid Monte Carlo samples (λ, μ, ν).

depicts the convergence domain of the system according to the hard constraints argued in Section IV. The subset of the database consists of half the right hand samples of all the subjects acquired in the spectrum band at 940 nm, whilst the number of parameter sets (λ, μ, ν) generated by the Monte Carlo sampling and belonging to the convergence domain is equal to 176. Hence, the amount of the tests performed is $176 \times \binom{300}{2} = 7\,893\,600$. Figure 4 illustrates a comparative analysis of the performance by plotting the genuine acceptance rate against the false acceptance rate for several different parameter sets (λ, μ, ν), whilst Table 2 presents detailed results in terms of equal error rate and genuine acceptance rate achieved by each parameter set.

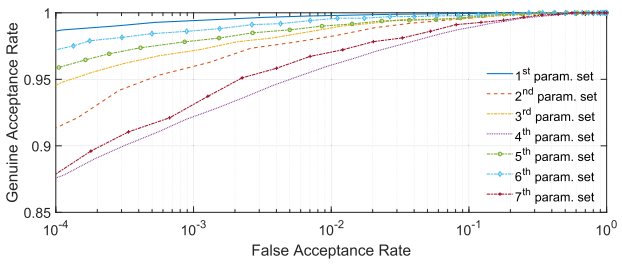

FIGURE 4. Comparative graph of several ROC curves generated by plotting the Genuine Acceptance Rate against False Acceptance Rate obtained using different parameter configurations.

It is worth of note that to verify the effectiveness and robustness of our system, the parameters obtained from the test conducted using images acquired under 940 nm wavelength illumination have been used for the verification experiments on both the testing databases using different wavelength illumination images without parameter re-tuning. Thus, the best parameter values resulting from the simulation are:

$$\begin{cases} \lambda = 630 \cdot 10^{-3} \\ \mu = 295 \cdot 10^{-4} \\ \nu = 292 \cdot 10^{-3}. \end{cases} \tag{20}$$

To limit the computational cost of the matching process, it is important to set a priori the number of iterations after

TABLE 2. Comparative analysis of the performance in terms of equal error rate and genuine acceptance rate using the subset of the CASIA database considering the near-infrared spectrum band at 940 nm.

	Parameter set						
	1st	2nd	3rd	4th	5th	6th	7th
EER [%]	0.23	1.46	1.02	2.53	0.98	0.65	1.99
GAR [%]	99.8	98.5	99.0	97.5	99.0	99.4	98.0

which we can consider the response close enough to the steady state of the dynamic system. Hence, to better illustrate the behaviour of the system in terms of accuracy, even with respect to our previous algorithm for palmprint matching [25], we performed the tests executing the algorithms with a large number of iterations, thus allowing the systems to reach the steady state condition.

We used the results from the tests obtained using the proposed approach and our previous algorithm to graph their behaviours in terms of discriminating power. Figure 5 illustrates the difference between the mean values of the true positive and true negative rates against the number of iterations, whilst the vertical dashed line represents the selected number of iterations at which the proposed system is intended to operate.

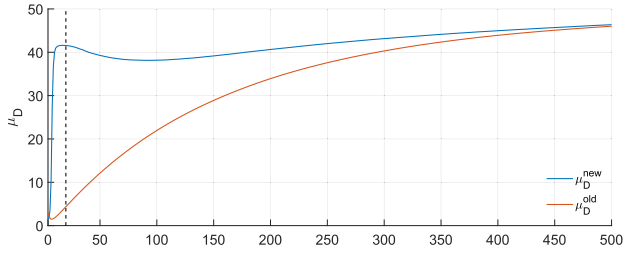

FIGURE 5. Comparison between the proposed approach and our previous algorithm in terms of discriminating power by plotting the difference between the mean values of the true positive and true negative rates against the number of iterations.

The figure clearly shows that, within a few iterations, the matching score achieved by the proposed system can be considered close enough to the convergence value of the dynamic system in the steady state condition. These results consistently suggests that the new approach achieves significantly improved performance over the one in [25], ensuring also greater reliability thanks to its higher discriminating power. Hence, to save computation time, the number of iterations for the tests has been set to 15.

C. PERFORMANCE ASSESSMENT AND COMPARISON

In order to evaluate the accuracy of the proposed authentication method based on a single-sample approach for single biometric systems, each sample in the database has undergone a one-to-one matching test against every single stored sample. Hence, a comparison between a subject with real identity I_r and a subject with claimed identity I_c is aimed at testing the hypothesis:

$$H_0 : I_r = I_c \quad \text{versus} \quad H_1 : I_r \neq I_c \tag{21}$$

where H_0 is the null hypothesis that the user is who s/he claims to be (genuine or intra-class matching), whilst H_1 is the alternative hypothesis that the user is not who s/he claims to be (impostor or inter-class matching). In particular, given a threshold value, t, all matching values lower than t lead to the rejection of the null hypothesis H_0 [6]. Therefore, whether the hypothesis is accepted or rejected, the test is subject to two kinds of errors:

1) False Acceptance Rate (FAR) that is the probability of accepting the null hypothesis H_0 when input is not valid,
2) False Rejection Rate (FRR) that is the probability of rejecting the null hypothesis H_0 when input is valid.

The Genuine Acceptance Rate (GAR) is instead the probability of accepting the null hypothesis H_0 when input is valid. The Receiver Operating Characteristic (ROC) represents the trade-off between FAR and FRR when the threshold varies, whilst the intersection point for which rejection and acceptance errors are equal is named Equal Error Rate (EER).

In our experiments, we have performed tests by taking 12 samples in the NIR spectrum at 880 nm of the left and right hands of all the subjects from the *PolyU multispectral palmprint database* and 6 samples in the NIR spectrum at 850 nm of the left and right hands of all the subjects from the *CASIA multispectral palmprint database*, for a total of 6 000 and 1 200 samples, respectively. Furthermore, in order to increase the amount of intra-class tests and to comparatively assess the performance from various approaches, we regarded both hands as belonging to different subjects [1], [2], [16], [21], [26], [28]. As a matter of fact this setup constitutes a total number of experiments equal to: 1) $\binom{6\,000}{2} = 17\,997\,000$, including $2 \times 250 \times \binom{12}{2} = 33\,000$ intra-class experiments for the PolyU database, and 2) $\binom{1200}{2} = 719\,400$, including $2 \times 100 \times \binom{6}{2} = 3\,000$ intra-class experiments for the CASIA database.

Figure 6(a) and Figure 6(b) outline the trade-off between the FRR and the FAR curves when the threshold varies, whilst the two EERs identified by the intersection point between the curves are $2.341 \cdot 10^{-5}$ for the PolyU database and $1.081 \cdot 10^{-3}$ for the CASIA database. Figure 6(c) and Figure 6(d) instead, illustrate the genuine (intra-class) and impostor (inter-class) distributions for both the databases. The two distributions (or classes) are clearly separated in both the databases, indicating the ability of the system to distinguish the genuine user samples from those of the impostors. Indeed, the separation also provides a hint on the threshold point that maximises the variance between the two classes in order to correctly mark a user sample image as authentic or impostor.

To assess the performance of the proposed dynamic palm vein matching (DPVM) system with respect to several

TABLE 3. Summary of the performance in terms of EER derived from several published methods.

Reference	Year	Database (DB)			Methodology		EER
		Name	Users	Samples	Features	Matching	[%]
Zhou *et al.* [31]	2011	CASIA	200	6	Neighborhood Matching Radon Transform	Hamming distance	0.51
					Hessian phase	Hamming distance	1.44
		PolyU	500	12	Neighborhood Matching Radon Transform	Hamming distance	0.004
					Hessian phase	Hamming distance	0.43
Sun *et al.* [26]	2012	PolyU	500	12	Curvelet transform	Hamming distance	0.66
Al-juboori *et al.* [1]	2013	PolyU	500	12	Gabor filters and FDA	Single nearest neighbours	0.2335
Kang *et al.* [15]	2014	CASIA	100	6	Mutual foreground LBP	χ^2 distance	2.53
					Mutual foreground LBP	χ^2 distance and SVM score fusion	0.267
Hong *et al.* [16]	2015	CASIA	200	6	RootSIFT	LBP-based mismatching removal	0.996
Wang *et al.* [28]	2017	PolyU	500	12	Discriminative LBP	χ^2 distance	0.079
Ma *et al.* [21]	2017	CASIA	200	6	Adaptive Gabor filter	Normalised Hamming distance	0.12
Ahmad *et al.* [2]	2019	PolyU	500	12	Wave atom transform	Normalised Hamming distance	1.98
Proposed method (DPVM)		CASIA	200	6	Morphological operations and LoG filter	Dynamical system	0.108
		PolyU	500	12	Morphological operations and LoG filter	Dynamical system	0.002

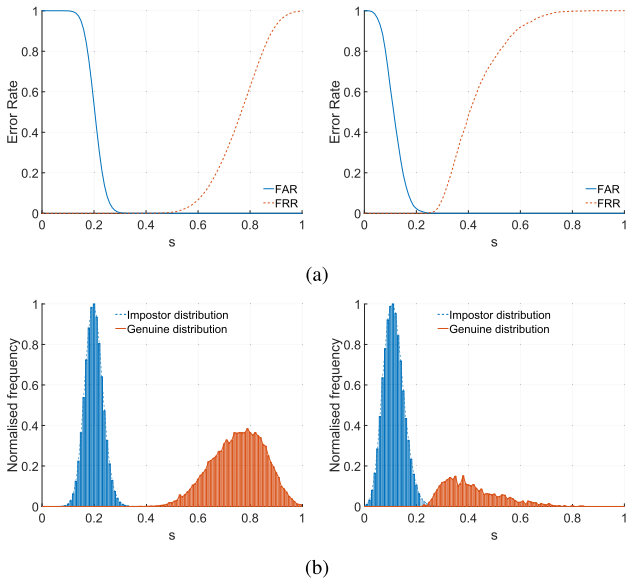

FIGURE 6. Performance assessment from PolyU (first coloumn) and CASIA (second coloumn) databases: (a) False Acceptance Rate and False Rejection Rate curves, and (b) estimation of theortical genuine and impostor distributions.

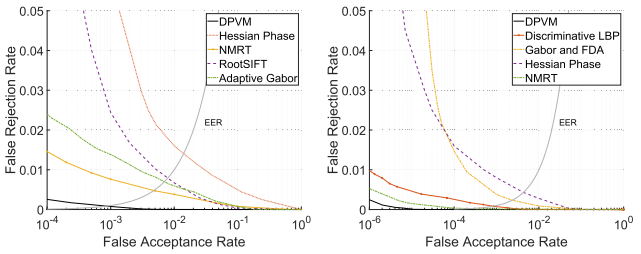

FIGURE 7. Comparison of detection error trade-off (DET) curves between the proposed system and other algorithms using (a) CASIA database and (b) PolyU database.

other approaches present in literature, we have presented in Figure 7 a comparison of the detection error trade-off (DET) curves, which have been drawn by plotting FRR against FAR. As the FRR indicates the number of match errors, the closer the curve is to the bottom of the graph, the better the biometric performance of the system. Hence, from Figure 7 it is clear that the dynamic palm vein matching algorithm has achieved better performance with regard to all the other methods, obtaining a GAR at FAR $= 10^{-6}$ equal to $\text{GAR}|_{\text{FAR}=10^{-6}} = 9.99 \cdot 10^{-1}$ and $\text{GAR}|_{\text{FAR}=10^{-6}} = 9.78 \cdot 10^{-1}$ for the PolyU and CASIA databases, respectively. Table 3 presents a summary of the performance in terms of equal error rate (EER) of different approaches in literature. In particular, our system has achieved a Zero False Acceptance Rate (ZeroFAR) and a Zero False Rejection Rate (ZeroFRR), which represent the FRR (resp. FAR) value when FAR (resp. FRR) is zero, equal to $\text{FRR}|_{\text{FAR}=0} = 5.57 \cdot 10^{-5}$ and $\text{FAR}|_{\text{FRR}=0} = 3.03 \cdot 10^{-5}$ for the PolyU database, and $\text{FRR}|_{\text{FAR}=0} = 1.96 \cdot 10^{-3}$ and $\text{FAR}|_{\text{FRR}=0} = 4.27 \cdot 10^{-2}$ for the CASIA database. Thus, these results show that our algorithm outperforms all the other approaches with an EER reduced at least by 50% with respect to the listed techniques, demonstrating the effectiveness of the proposed approach.

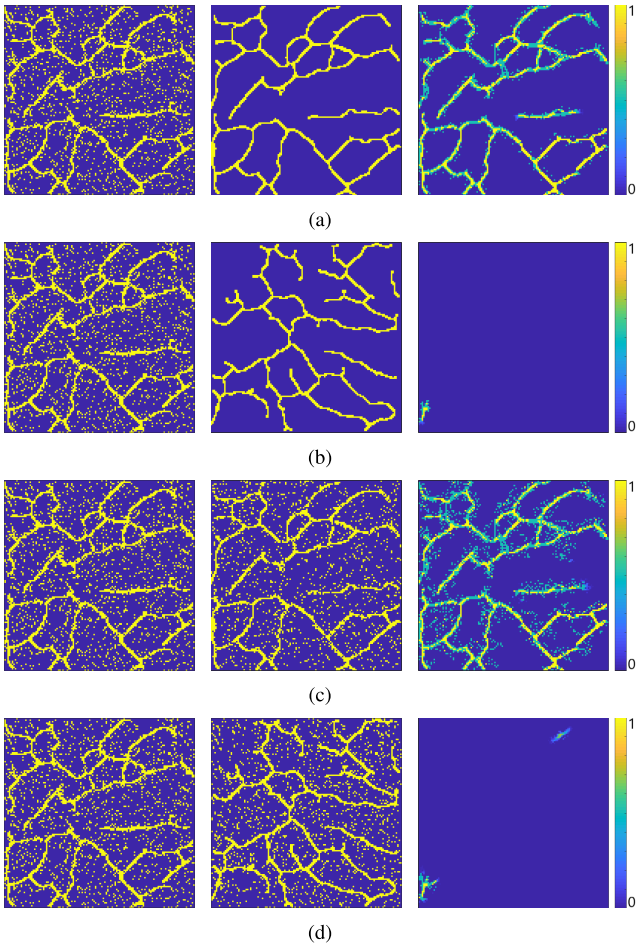

FIGURE 8. Dynamic algorithm behaviour in presence of random impulse noise with probability $p = 20\%$: a) true positive match with one image corrupted by noise, b) true negative match with one image corrupted by noise, c) true positive match with both images corrupted by noise, and d) true negative match with both images corrupted by identical noise (i.e., the same corrupted pixels).

D. NOISE IMMUNITY

To demonstrate the robustness of the dynamic algorithm against noise, further experiments have been carried out to compare normal images and images highly corrupted by random impulse noise. The model of this noise is always independent, randomly distributed, and uncorrelated with the images and can be described as follows:

$$I_n(x,y) = \begin{cases} 2^8 - 1 & \text{with probability} \quad p, \\ I(x,y) & \text{with probability} \quad 1-p. \end{cases} \tag{22}$$

Furthermore, the system robustness has also been tested performing impostor matching experiments by adding the same random impulse noise to the user sample images. These experiments lead to low matching scores because there are not enough connections between the active points of both the images to be compared (i.e., half of the points in the complementary neighbourhood are not active), though the pixels affected by noise are the same. As a result, the amount of survived points after the algorithm evolution is very limited. Figure 8 illustrates the dynamic algorithm behaviour in presence of random impulse noise with probability p equal to 20%. In particular the first column shows the user sample images to compare, the second column shows the user sample images of the claimed identity, and the last column shows the remaining points after the algorithm evolution. Four most significant examples have been reported, testing the following conditions: a) true positive match with the user sample image corrupted by noise, b) true negative match with the user sample image corrupted by noise, c) true positive match with both the images to be compared corrupted by noise, and d) true negative match with both the images to be compared corrupted by identical noise (i.e., the same corrupted pixels). These tests demonstrate that the system is able to recognise a subject with ease even if the samples are highly affected by noise. The video included in the additional material shows (tests #5 to #7) the system behaviour in noisy conditions.

E. COMPUTATIONAL EFFICIENCY

The experiments have been performed making use of a virtual machine configured with two dedicated processors and 4096 MB RAM hosted on an Intel Core i5-7200U CPU (2.5 GHz) with 8192 MB RAM running a 64-bit Microsoft Windows 10 operating system. The code has been implemented using Matlab R2016b; to estimate the total computation time, each part of the code has been performed 500 times, then it has been considered the mean time. As a result, the average computation times required for preprocessing, feature extraction, and matching of the proposed algorithm are 81 ms, 28 ms, 126 ms respectively. Hence, the mean response time for verification is about 0.235 s, making this approach suitable to be used in a real-time biometric authentication or identification system. The proposed template consists of a square Boolean matrix of dimensions 128×128 pixels, hence the total size for each template is 2048 bytes. In terms of algorithm particularities and user friendliness (the number of enrollment samples required), the system is computationally simple because it only requires one image as an enrollment template. This makes the algorithm well suited even for systems with limited resources.

VI. CONCLUSION

In this paper, a new approach for near-infrared subcutaneous palm vascular pattern authentication has been investigated. Inspired by our previous study [25], which adopts a dynamic algorithm tailored to palmprint features acquired in the visible electromagnetic spectrum rather than in the near-infrared, we have proposed a novel dynamical system approach achieving significantly improved performance over the earlier proposed system ensuring also greater reliability thanks to its higher discriminating power which allows to recognise a subject with ease, even if the templates are highly corrupted by noise. To evaluate the performance of the system a massive campaign of experiments has been conducted and the results clearly show that the proposed approach can compete with the state-of-the-art methods, achieving an EER equal to $1.081 \cdot 10^{-3}$ for the CASIA database and $2.341 \cdot 10^{-5}$ for

the PolyU database. The experiments presented in Section V illustrate that the value of GAR still can be considered 100% for levels of FAR up to 10^{-4} on the CASIA database and up to 10^{-6} on the PolyU database. In particular, setting the threshold such that the system works at ZeroFAR, the probability to reject a legitimate subject is $5.57 \cdot 10^{-5}$ for the PolyU database and $1.96 \cdot 10^{-3}$ for the CASIA database, whilst there is no likelihood of accepting impostors. We also want to highlight that the system has undergone a parameter tuning step which is required only once and there is no need to perform this phase again, even using different databases with different wavelength illumination images, which proves the effectiveness and robustness of the proposed system. In terms of algorithm particularities and user friendliness, the system is computationally simple and extremely fast (allowing for real-time applications) and user friendly, since it only requires one near-infrared image as an enrollment template. The computational time indeed requires only 0.235 s for the entire process, whilst the size of a single template is equal to 2048 bytes, thus allowing the use of the proposed method in systems with limited resources. Furthermore, the values of FAR, FRR and consequently of GAR obtained from the experimental results allow the system to meet the strict requirements of very high security applications.

ACKNOWLEDGMENT

The authors would like to thank the Hong Kong Polytechnic University (PolyU) and the Chinese Academy of Sciences Institute of Automation (CASIA) for providing the multispectral palmprint databases.

REFERENCES

[1] A. M. Al-Juboori, W. Bu, X. Wu, and Q. Zhao, "Palm vein verification using Gabor filter," *Int. J. Comput. Sci. Issues*, vol. 10, no. 1, pp. 678–684, 2013.

[2] F. Ahmad, L. Cheng, and A. Khan, "Lightweight and privacy-preserving template generation for palm-vein-based human recognition," *IEEE Trans. Inf. Forensics Security*, vol. 15, pp. 184–194, 2020.

[3] J. Canny, "A computational approach to edge detection," *IEEE Trans. Pattern Anal. Mach. Intell.*, vol. 8, no. 6, pp. 679–698, Nov. 1986.

[4] H. Chen, G. Lu, and R. Wang, "A new palm vein matching method based on ICP algorithm," in *Proc. 2nd Int. Conf. Interact. Sci. Inf. Technol., Culture Hum. (ICIS)*, 2009, pp. 1207–1211.

[5] R. Das, E. Piciucco, E. Maiorana, and P. Campisi, "Convolutional neural network for Finger-Vein-Based biometric identification," *IEEE Trans. Inf. Forensics Security*, vol. 14, no. 2, pp. 360–373, Feb. 2019.

[6] S. C. Dass, Y. Zhu, and A. K. Jain, "Validating a biometric authentication system: Sample size requirements," *IEEE Trans. Pattern Anal. Mach. Intell.*, vol. 28, no. 12, pp. 1319–1902, Dec. 2006, doi: 10.1109/TPAMI.2006.255.

[7] M. Fang, G. Yue, and Q. Yu, "The study on an application of otsu method in canny operator," in *Proc. Int. Symp. Inf. Process.*, 2009, pp. 109–112.

[8] R. Garnett, T. Huegerich, C. Chui, and W. He, "A universal noise removal algorithm with an impulse detector," *IEEE Trans. Image Process.*, vol. 14, no. 11, pp. 1747–1754, Nov. 2005.

[9] D. Hong, W. Liu, J. Su, Z. Pan, and G. Wang, "A novel hierarchical approach for multispectral palmprint recognition," *Neurocomputing*, vol. 151, pp. 511–521, Mar. 2015.

[10] L. Hong, Y. Wan, and A. Jain, "Fingerprint image enhancement: Algorithm and performance evaluation," *IEEE Trans. Pattern Anal. Mach. Intell.*, vol. 20, no. 8, pp. 777–789, Aug. 1998.

[11] D. Huang, Y. Tang, Y. Wang, L. Chen, and Y. Wang, "Hand-dorsa vein recognition by matching local features of multisource keypoints," *IEEE Trans. Cybern.*, vol. 45, no. 9, pp. 1823–1837, Sep. 2015.

[12] A. K. Jain, A. Ross, and S. Prabhakar, "An introduction to biometric recognition," *IEEE Trans. Circuits Syst. Video Technol.*, vol. 14, no. 1, pp. 4–20, Jan. 2004.

[13] Z. Khan, A. Mian, and Y. Hu, "Contour code: Robust and efficient multispectral palmprint encoding for human recognition," in *Proc. Int. Conf. Comput. Vis.*, Nov. 2011, pp. 1935–1942.

[14] A. Kumar, M. Hanmandlu, and H. M. Gupta, "Online biometric authentication using hand vein patterns," in *Proc. IEEE Symp. Comput. Intell. Secur. Defense Appl.*, Jul. 2009, pp. 1–7.

[15] W. Kang and Q. Wu, "Contactless palm vein recognition using a mutual foreground-based local binary pattern," *IEEE Trans. Inf. Forensics Security*, vol. 9, no. 11, pp. 1974–1985, Nov. 2014.

[16] W. Kang, Y. Liu, Q. Wu, and X. Yue, "Contact-free palm-vein recognition based on local invariant features," *PLoS ONE*, vol. 9, no. 5, 2014, Art. no. e97548.

[17] A. Kong, D. Zhang, and M. Kamel, "A survey of palmprint recognition," *Pattern Recognit.*, vol. 42, no. 7, pp. 1408–1418, Jul. 2009.

[18] W. Luo, "Efficient removal of impulse noise from digital images," *IEEE Trans. Consum. Electron.*, vol. 52, no. 2, pp. 523–527, May 2006.

[19] C.-L. Lin and K.-C. Fan, "Biometric verification using thermal images of palm-dorsa vein patterns," *IEEE Trans. Circuits Syst. Video Technol.*, vol. 14, no. 2, pp. 199–213, Feb. 2004.

[20] L. Lam, S. Lee, and C. Y. Suen, "Thinning methodologies-a comprehensive survey," *IEEE Trans. Pattern Anal. Mach. Intell.*, vol. 14, no. 9, pp. 869–885, Sep. 1992.

[21] X. Ma, X. Jing, H. Huang, Y. Cui, and J. Mu, "Palm vein recognition scheme based on an adaptive Gabor filter," *IET Biometrics*, vol. 6, no. 5, pp. 325–333, Sep. 2017.

[22] N. Miura, A. Nagasaka, and T. Miyatake, "Feature extraction of finger-vein patterns based on repeated line tracking and its application to personal identification," *Mach. Vis. Appl.*, vol. 15, no. 4, pp. 194–203, Oct. 2004.

[23] E. Piciucco, E. Maiorana, and P. Campisi, "Palm vein recognition using a high dynamic range approach," *IET Biometrics*, vol. 7, no. 5, pp. 439–446, Sep. 2018.

[24] D. Palma, P. L. Montessoro, G. Giordano, and F. Blanchini, "A dynamic algorithm for palmprint recognition," in *Proc. IEEE Conf. Commun. Netw. Secur. (CNS)*, Sep. 2015, pp. 659–662.

[25] D. Palma, P. L. Montessoro, G. Giordano, and F. Blanchini, "Biometric palmprint verification: A dynamical system approach," *IEEE Trans. Syst., Man, Cybern., Syst.*, vol. 49, no. 12, pp. 2676–2687, Dec. 2019.

[26] J. Sun and W. Abdulla, "Palm vein recognition using curvelet transform," in *Proc. 27th Conf. Image Vis. Comput. New Zealand (IVCNZ)*, 2012, pp. 435–439.

[27] L. Wang, G. Leedham, and S.-Y. Cho, "Infrared imaging of hand vein patterns for biometric purposes," *IET Comput. Vis.*, vol. 1, no. 3, pp. 113–122, Dec. 2007.

[28] J. Wang and G. Wang, "Quality-specific hand vein recognition system," *IEEE Trans. Inf. Forensics Security*, vol. 12, no. 11, pp. 2599–2610, Nov. 2017.

[29] X. Yan, W. Kang, F. Deng, and Q. Wu, "Palm vein recognition based on multi-sampling and feature-level fusion," *Neurocomputing*, vol. 151, pp. 798–807, Mar. 2015.

[30] D. Zhang, Z. Guo, G. Lu, L. Zhang, Y. Liu, and W. Zuo, "Online joint palmprint and palmvein verification," *Expert Syst. Appl.*, vol. 38, no. 3, pp. 2621–2631, Mar. 2011.

[31] Y. Zhou and A. Kumar, "Human identification using palm-vein images," *IEEE Trans. Inf. Forensics Security*, vol. 6, no. 4, pp. 1259–1274, Dec. 2011.

[32] D. Zhang, W.-K. Kong, J. You, and M. Wong, "Online palmprint identification," *IEEE Trans. Pattern Anal. Mach. Intell.*, vol. 25, no. 9, pp. 1041–1050, Sep. 2003.

[33] X. Zhou, K. Zhou, and L. Shen, "Rotation and translation invariant palmprint recognition with biologically inspired transform," *IEEE Access*, vol. 8, pp. 80097–80119, 2020.

[34] Biometric Research Centre of the Hong Kong Polytechnic University. *PolyU Multispectral Palmprint Database*. Accessed: Jun. 2019. [Online]. Available: http://www.comp.polyu.edu.hk/~biometrics/MultispectralPalmprint/MSP.htm

[35] Chinese Academy of Sciences Institute of Automation. *CASIA Multi-Spectral Palmprint Image Database V1.0*. Accessed: Jun. 2019. [Online]. Available: http://biometrics.idealtest.org/

DAVID PALMA (Graduate Student Member, IEEE) received the B.Sc. and M.Sc. degrees from the University of Udine, Italy, in 2014 and 2017, respectively, where he is currently pursuing the Ph.D. degree in industrial and information engineering with the Distributed and Dynamical Systems Research Group. Since 2015, he has been a Research Assistant and an Assistant Lecturer in computer and network security with the University of Udine. In 2019, he was a Visiting Ph.D. Researcher with the Control and Power Research Group, Imperial College London, U.K. His current research interests include digital signal and image processing, dynamical systems, intelligent control, and pattern recognition with applications in different security-related areas, in particular biometrics and cyber-physical systems security.

FRANCO BLANCHINI (Senior Member, IEEE) was born in Legnano, Italy, in December 1959. He is currently the Director of the Laboratory of System Dynamics, University of Udine. He has been involved in the organization of several international events, including the Program Vice-Chair of the 2005 Joint IEEE Conference on Decision and Control and European Control Conference (CDC-ECC), the 2008 CDC, the 2013 CDC, and the Program Chair of the 2012 IFAC Symposium on Robust Control Design (ROCOND). He is the coauthor of the book *Set Theoretic Methods in Control* (Birkhauser). He received the 2001 ASME Oil and Gas Application Committee Best Paper Award, as a coauthor of the article, Experimental Evaluation of a High-Gain Control for Compressor Surge Instability, the 2002 *Automatica* Paper Prize for Set Invariance in Control—A Survey, the IFAC High Impact Paper Award for the latter article, in 2017, and the Nonlinear Analysis and Hybrid Systems Best Paper Award, as a coauthor of the article, A Switched System Approach to Dynamic Race Modelling, in 2017. He served as an Associate Editor for *Automatica*, from 1996 to 2006, the IEEE TRANSACTIONS ON AUTOMATIC CONTROL, from 2012 to 2016, and *Automatica*, from 2017 to 2019. He was a Senior Editor of the IEEE CONTROL SYSTEMS SOCIETY LETTERS, from 2017 to 2018.

GIULIA GIORDANO (Member, IEEE) received the B.Sc. and M.Sc. degrees *summa cum laude* in electrical engineering and the Ph.D. degree (Hons.) in systems and control theory from the University of Udine, Italy, in 2010, 2012, and 2016, respectively. She visited the Control and Dynamical Systems Group, California Institute of Technology, Pasadena, CA, USA, in 2012, and the Institute of Systems Theory and Automatic Control, University of Stuttgart, Germany, in 2015. She was a Research Fellow with the LCCC Linnaeus Center and the Department of Automatic Control, Lund University, Sweden, from 2016 to 2017. She was a Faculty Member with the Delft Center for Systems and Control, Delft University of Technology, The Netherlands, from 2017 to 2019. She is currently an Assistant Professor with the Department of Industrial Engineering, University of Trento, Italy. Her main research interests include study of dynamical networks, analysis of biological systems, and the control of networked systems. She received the Outstanding Reviewer Letter from the IEEE TRANSACTIONS ON AUTOMATIC CONTROL, in 2016, the EECI Ph.D. Award from the European Embedded Control Institute for her thesis Structural Analysis and Control of Dynamical Networks, in 2016, the NAHS Best Paper Prize 2017, as the coauthor of the article, A Switched System Approach to Dynamic Race Modelling, Nonlinear Analysis: Hybrid Systems, in 2016, the Delft Technology Fellowship, in 2018, and the NWO Talent Programme Veni, in 2019.

PIER LUCA MONTESSORO (Member, IEEE) was born in Torino, Italy, in 1961. He received the Dr.Eng. degree in electronic engineering from the Polytechnic of Turin, Italy, in 1986. He was with the Italian National Council for Scientific Research, Italy, and the Scientific Consultant for the Digital Equipment Corporation (Compaq), Maynard, MA, USA, in the field of simulation for VLSI design. He is currently a Full Professor in computer science with the University of Udine, Italy. His research interests include CAD systems for digital circuits design, multimedia systems for tele-teaching, e-learning, computer networks and ICT security, and pervasive computing, in particular distributed controls and algorithms for agents-based systems. He was the Chair and an Organizer of the WCC 2013 Workshop International Workshop on Cloud Convergence: Challenges for Future Infrastructures and Services, hosted in the IEEE ICC Conference, and the Chair of the 30th Edition of the Didamatica Conference, Udine. He received the Best Paper Award for the Paper, A Distributed Algorithm for Efficient and Scalable Resource Booking Management, CTRQ 2010, and the Third International Conference on Communication Theory, Reliability, and Quality of Service.